Shedding dynamics and mass exchange by dry granular waves flowing over erodible beds

S Viroulet, a N Edwards, C G Johnson, B P Kokelaar, J M N T Gray

Earth and Planetary Science Letters 523 (2019) 115700

Contents lists available at ScienceDirect

Earth and Planetary Science Letters

www.elsevier.com/locate/epsl

Shedding dynamics and mass exchange by dry granular waves flowing over erodible beds

S. Viroulet [a,*], A.N. Edwards [b], C.G. Johnson [b], B.P. Kokelaar [c], J.M.N.T. Gray [b]

[a] Institut de Mécanique des Fluides de Toulouse (IMFT) - Université de Toulouse, CNRS, Toulouse, France
[b] School of Mathematics and Manchester Centre for Nonlinear Dynamics, University of Manchester, Manchester, M13 9PL, UK
[c] Department of Earth and Ocean Sciences, University of Liverpool, Liverpool, L69 3GP, UK

ARTICLE INFO

Article history:
Received 15 December 2018
Received in revised form 27 June 2019
Accepted 1 July 2019
Available online 22 July 2019
Editor: W.B. McKinnon

Keywords:
granular flow
erosion-deposition waves
runout distance

ABSTRACT

A continuous exchange of particles between an erodible substrate and the granular flow above it occurs during almost all geophysical events involving granular material, such as snow avalanches, debris flows and pyroclastic flows. The balance between eroded and deposited material can drastically influence the runout distance and duration of the flow. In certain conditions, a perfect balance between erosion and deposition may occur, leading to the steady propagation of material, in which the flow maintains its shape and velocity throughout. It is shown experimentally how the erosion-deposition process in dense flows of sand (160-200 μm) on an erodible bed of the same material produces steadily propagating avalanches that deposit subtle levees at their lateral extent. Moreover, it is shown in this paper, by using two colours of the same sand, that although the avalanche is propagating at constant velocity and maintaining a constant shape, the grains that are initially released are deposited along the flow path and that the avalanche will eventually be composed entirely of particles that are eroded from the bed. Different steady travelling wave regimes are obtained depending on the slope angle, thickness of the erodible layer and the amount of material released. Outside of the range of parameters where steady travelling waves form, the avalanches loose mass and decay if the initial amount of material released is too small, or, if the initial release is too large, they re-adjust to a steadily propagating regime by shedding material and breaking into smaller avalanches at its rear side. Numerical simulations are performed using a shallow-water-like avalanche model together with a friction law that captures the erosion-deposition process in flowing to static regimes and a transport equation for the interface between layers of the two colours. The characteristic behaviours observed in the experiments are qualitatively reproduced. Specifically, the complex processes such as the exchange of particles leading to a change in colour of the avalanche and the formation of lateral levees are captured by the model. Finally a comparison is made with deposits in lunar craters, which are interpreted as closely analogous to the deposits formed in our laboratory experiments.

1. Introduction

Debris flows, rock avalanches and pyroclastic flows are some common examples of dense, geophysical, granular flows that occur on relatively steep slopes. During the past thirty years, a number of important studies have improved our understanding of such flows and their applications to geophysical events. Interaction with topography has been widely studied since the seminal work of Savage and Hutter (1991) and has been extended to more complex topographies (Gray et al., 1999; Bouchut and Westdickenberg, 2004; Viroulet et al., 2017), as well as implemented in numerical models to simulate real events (Kelfoun and Druitt, 2005; Mangeney et al., 2007; Moretti et al., 2015).

Natural granular flows usually exhibit a high degree of polydispersity, with mean particle diameters spanning several orders of magnitude. Size-segregation can lead to the formation of regions that have different frictional properties, which feedback on the flow. The finger-like deposit observed after a volcanic eruption, for example, is mainly due to the differential particle size and roughness (Pouliquen et al., 1997). This mechanism was later studied analytically and numerically (Gray and Thornton, 2005; Woodhouse et al., 2012; Baker et al., 2016b) with application to large scale experiments (Johnson et al., 2012). Moreover, it has recently been shown that the runout distance of geophysical flows may be enhanced by the creation of fine grain-lined, leveed chan-

* Corresponding author.
E-mail address: sylvain.viroulet@imft.fr (S. Viroulet).

https://doi.org/10.1016/j.epsl.2019.07.003

nels (Kokelaar et al., 2014). Despite these and many other studies (see Delannay et al., 2017 for a review), rheological behaviour of granular flows and their application to natural flows is still an open question.

In particular, there is a lack of understanding of the effects of erosion and deposition in granular flows, despite its key role in the flow behaviour and the significant effects it can produce. Insights from field measurements of geophysical flows are relatively poor due to the difficulty of taking such measurements (Conway et al., 2010; Iverson et al., 2011). Direct measurement of channel erosion by successive debris flows was performed by Berger et al. (2011). It has been shown that erosion took place at the head of the flow and deposition at a later stage. Moreover, the flow consisted of several surges with channel bed sediment entrained at the head of the flow. This field observation can also be directly linked to small scale experiments on erosion/deposition waves (Edwards and Gray, 2015) and bidisperse granular roll waves (Viroulet et al., 2018). Numerous laboratory experiments of granular flows on erodible beds have been performed using, for example, a column collapse configuration (Mangeney et al., 2010; Farin et al., 2014), a constant inflow that develops into erosion-deposition waves (Edwards and Gray, 2015), or the release of a small number of grains on a stationary layer of the same material at a steep inclination (Pouliquen and Forterre, 2002; Edwards et al., 2017). All of these studies showed a significant increase in the runout distance and flow duration in the presence of an erodible layer.

A major difficulty in simulating such experiments is the understanding of the rheological behaviour of the granular material. Whilst a simple Mohr-Coulomb friction law can produce good results for accelerating flows on smooth beds (Cui and Gray, 2013; Viroulet et al., 2017), granular flows are better described by viscoplastic laws such as the $\mu(I)$-rheology of Jop et al. (2006). Recently, a depth-averaged $\mu(I)$-rheology has been developed by Gray and Edwards (2014) that introduces a depth-averaged viscous term into the equations. Using this approach, they were able to predict the frequency at which the growth rate of the roll-wave instability is zero (Forterre and Pouliquen, 2003; Forterre, 2006) without any fitting parameters. A generalisation of this model to two dimensions was later developed by Baker et al. (2016a) which predicts the downslope velocity profile across a channel and the formation of fingers (Baker et al., 2016b).

This paper focuses on small-scale experiments that exhibit the exchange and entrainment of particles between an erodible layer of grains and a steadily propagating granular avalanche. Experimental results are presented for the release of a small amount of grains on an erodible layer composed of the same material except coloured differently, allowing the particles from the original release to be visually tracked. The experiments are modelled using a depth-averaged framework based on that of Edwards et al. (2017) for decaying, growing or steadily propagating granular avalanches, together with Gray and Kokelaar's (2010) large-particle transport equation for the interface between the differently coloured layers. Numerical simulations are shown to capture the various avalanche behaviours and the exchange of particles with good qualitative agreement.

2. Experimental method

Experiments have been performed to visualize the exchange of grains during the erosion-deposition process and investigate the underlying physical mechanism in dry granular flows. The experimental setup consists of a 1.2 m long and 0.5 m wide plane inclined at an angle ζ to the horizontal. The slope is roughened by attaching a layer of coarse spherical ballotini (0.75–1 mm diameter) to the plane using double-sided sticky tape. The granular material used in these experiments is sieved sand with a 0.16–0.20 mm mean diameter that is coloured red or yellow. A static layer of erodible material is prepared before each experiment by releasing a finite mass of red sand from a hopper to produce a deposit of thickness $h_{stop}(\zeta)$ on a slope of angle ζ. For steady uniform flows there is a balance between gravity and shear stress at the bed, which implies that $\mu = \tan(\zeta)$ (Pouliquen, 1999b; Pouliquen and Forterre, 2002). By measuring the evolution of the deposit layer thickness as a function of the slope angle, the material properties can be defined by using the dynamic empirical friction law of Pouliquen and Forterre (2002) as

$$\tan(\zeta) = \tan\zeta_1 + \frac{\tan\zeta_2 - \tan\zeta_1}{1 + h_{stop}/\mathscr{L}}, \tag{1}$$

where ζ_1 and ζ_2 are critical angles of the material and $\mathscr{L}$ is a characteristic length over which a transition between ζ_1 and ζ_2 occurs. Values of these parameters are determined here by a best fit to average measurements of the thickness $h_{stop}(\zeta)$ on our experimental setup, shown in Fig. 2.

Furthermore, by measuring the velocity of the front of a steady uniform flow, additional material flow properties are determined by the dynamic flow rule of Forterre and Pouliquen (2003) for angular particles (e.g. sand and carborundum) as

$$\mathrm{Fr} = \frac{|\bar{\boldsymbol{u}}|}{\sqrt{gh\cos\zeta}} = \frac{\beta h}{h_{stop}} - \Gamma, \tag{2}$$

where the constant of proportionality $\beta = 0.63$ and $\Gamma = 0.40$ is the offset. These values of the flow rule properties are taken here from those measured by Edwards et al. (2017) for flows on a rough bed of 0.75–1 mm diameter spherical glass beads using carborundum particles, which are very similar in size and roughness to our sand. Values of all of the parameters used here are summarised in Table 1. With the static layer prepared, an avalanche is initiated by releasing a finite amount of the yellow sand by lifting a small filled cylinder that is placed on top of the red h_{stop} layer without disturbing it. A schematic representation of the experimental setup is shown in Fig. 1. The particles from the cylinder rapidly spread from

Table 1
Material properties kept constant throughout.

$\zeta_1 = 30.4°$	$\zeta_2 = 43.2°$	$\zeta_3 = 34.9°$	$\mathscr{L} = 0.56$ mm
$\beta = 0.63$	$\Gamma = 0.40$	$\beta_* = 0.47$	$\kappa = 1$

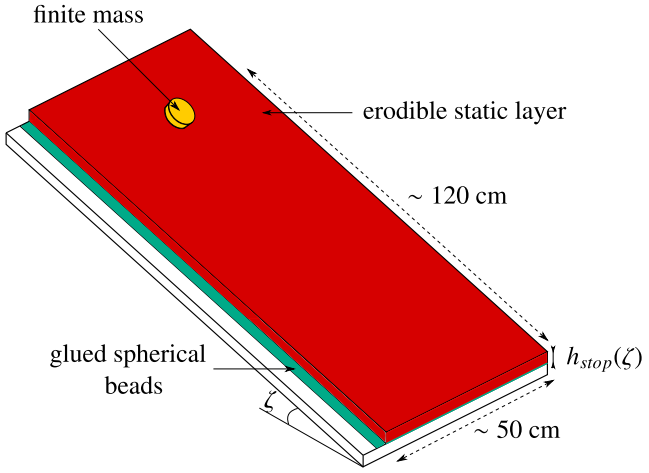

Fig. 1. Schematic diagram of the experimental setup. A finite cylindrical mass of yellow grains is released onto a static erodible layer of red sand with the same rheological properties. (For interpretation of the colours in the figure(s), the reader is referred to the web version of this article.)

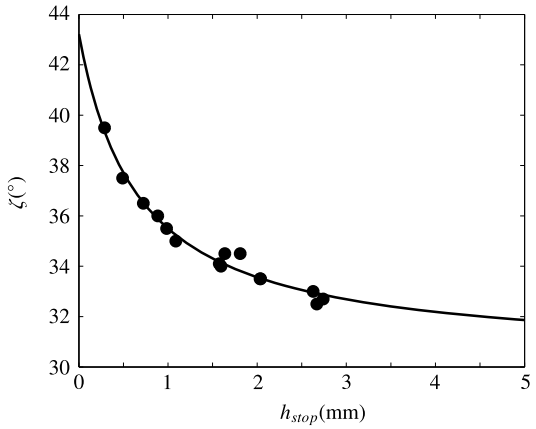

Fig. 2. Variation of the deposit thickness h_{stop} left by a steady uniform flow as a function of the slope angle ζ.

its downslope edge before forming an avalanche that travels down the plane by eroding particles from the static layer at the flow front and depositing particles behind. As soon as the avalanche forms a balance between erosion and deposition arises, with red particles being eroded from the static layer and yellow particles deposited behind. Illuminating the flow from the bottom of the plane creates a low-angled light that makes the avalanche shape clearly evident, in particular the levees, which are deposited at the lateral extents of the bulk head width. Depending on the slope inclination angle and thickness of the static layer, different characteristic behaviours are observed. The avalanche either grows by eroding progressively more particles from the static layer, decays in size until it comes to rest or travels steadily whilst maintaining a constant shape and velocity. Only the steadily propagating and decaying avalanches are considered in the remainder of this study, since a specific initial configuration of an abundantly thick h_{stop} layer, prepared at a shallower angle than that of the experiment, is needed to obtain a growing avalanche (see Edwards et al., 2017).

3. Experimental results

3.1. Redistribution of particles in a steadily propagating avalanche

The plane is inclined at an angle of 34.0° to the horizontal and a static layer of thickness $h_{stop}(34.0°) \approx 1.7$ mm is prepared according to §2. These conditions lead to the formation of a steadily propagating avalanche as long as a sufficient volume of grains is released. A cylinder filled with 10 mL of yellow sand is placed on top of the static layer of red-coloured sand. After the release, the grains rapidly spread and the flow adjusts itself to a width that remains constant thereafter. The evolution of the avalanche during its propagation is captured by an overhead camera and shown in Figs. 3b)–f). Near to the end of the chute, it can be seen that almost all of the initial yellow grains have been deposited behind the avalanche, which itself consists of mainly red particles. The levees are perfectly parallel, which implies that once a steadily travelling wave is established, the avalanche does not gain or loose mass and there is a perfect balance between erosion and deposition. To demonstrate the effects of providing an erodible substrate layer to an avalanche, the deposit left using the same amount of yellow sand on the rough, non-erodible bed of glass beads is shown in Fig. 3(a). As in previous studies (Pouliquen and Forterre, 2002; Mangeney et al., 2010; Edwards et al., 2017), the presence of an erodible layer considerably increases the runout distance of granular flows, i.e. erodible layers produce an apparent reduction in friction.

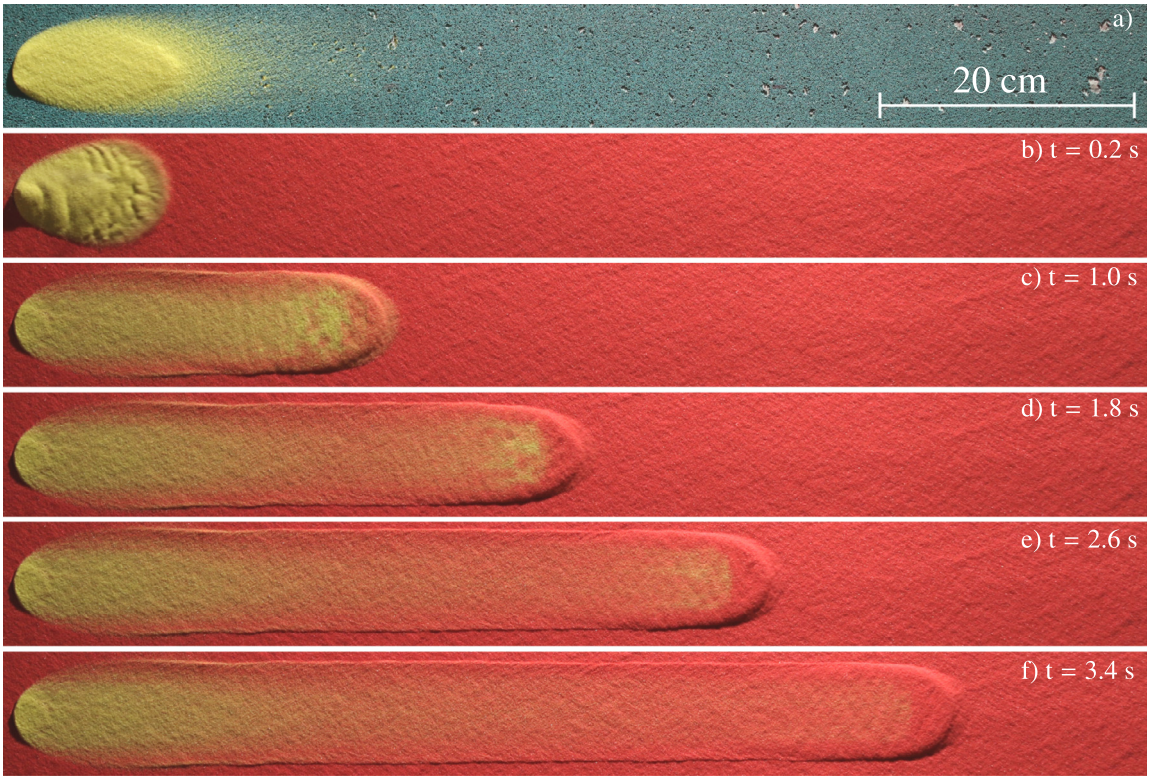

Fig. 3. Propagation of a single avalanche on a 34.0° slope. a) Deposit without an erodible layer. b)–f) Steady travelling wave propagating on an erodible layer of thickness $h_{stop}(34.0°) \approx 1.7$ mm. All of the initially released yellow sand is deposited during the flow, resulting in a steady avalanche that is composed entirely of red particles eroded from the bed. The same configuration is shown in movie 1 in the online supplementary material.

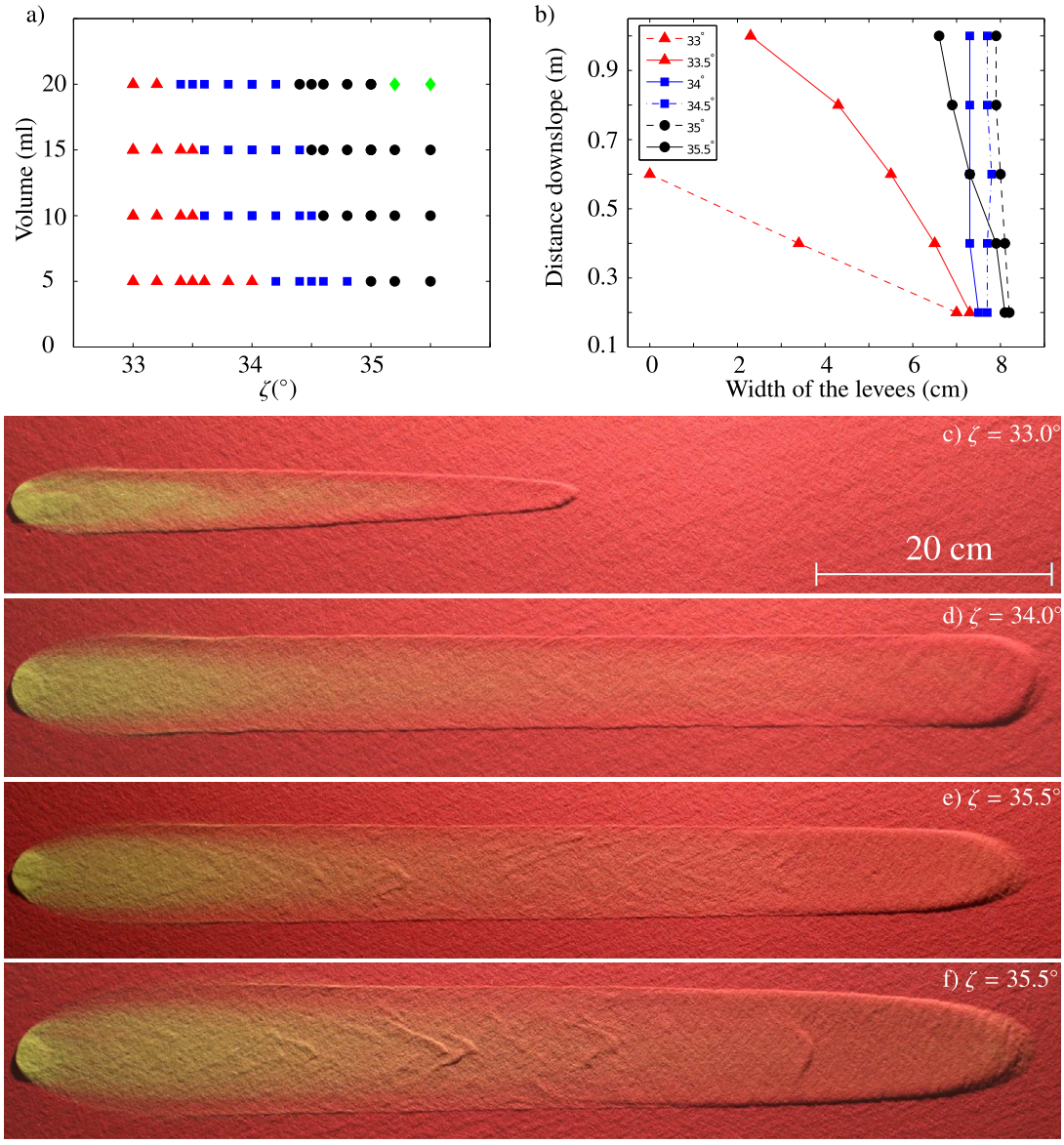

Fig. 4. a) Phase diagram showing the different avalanche behaviours as a function of the volume of grains released on an erodible layer and the slope angle. Decaying (red triangles), steady (blue squares), shedding (black circles) and extreme shedding avalanches with generation of secondary waves (green diamonds) are all observed. b) Evolution of the width of the levees deposited at the lateral extents of avalanches formed by a 10 mL release of grains at various slope angles. Typical experiments for each type of behaviour: c) 10 mL - decaying, d) 10 mL - steady, e) 10 mL - shedding and f) 20 mL - extreme shedding with secondary waves. All of the initial release of yellow sand is deposited during the propagation to produce avalanches that are composed entirely of particles eroded from the static layer of red sand. Movies of the experiments for each behaviour are available in the online supplementary material (movie 1 to 4).

3.2. Multiple steady-states and shedding of excess material

Various propagation regimes have previously been found by Edwards et al. (2017) dependent on the slope angle and the thickness of the erodible layer. In addition to this, steady travelling waves, which are referred to as steady-states hereafter, are possible for various slope angles and amounts of released material, even for the same erodible layer thickness $h_{stop}(\zeta)$ and slope angle ζ. For a given angle, a minimum amount of material is needed to generate an avalanche that is large enough to reach a steady-state. If the initial volume of material is too small, the avalanche will continuously decay and come to rest. However, once a steady-state is found, increasing the initial volume released at that slope angle will produce a different steady-state with a larger amplitude and width. The volume can be increased further to produce multiple sized steady-states regimes until the avalanche becomes too large to support itself and sheds excess material, which itself can break into several smaller avalanches, in order to re-adjust to a steady-state. This maximum volume for a steady avalanche is analogous to the maximum thickness of erosion-deposition waves observed by Edwards and Gray (2015). Moreover, taking a known steady propagating avalanche configuration and increasing the slope, thus decreasing the erodible layer thickness, whilst releasing the same volume of material also produces multiple steady-states, until the shedding and re-adjusting regime is reached at a sufficiently high inclination. Therefore, depending on the slope angle and the initial amount of material released, an avalanche either decays, propagates steadily or breaks and re-adjusts to a steady-state. For example, when a 10 mL volume of material released on an erodible layer of thickness $h_{stop}(\zeta)$, the avalanche will decay for $\zeta \leq 33.5°$, propagate steadily for $33.5 < \zeta \leq 34.5°$ and shed material for $\zeta > 34.5°$. A phase diagram of the different behaviours is shown in Fig. 4(a) for various slope angles and volumes of mass released.

Tracking the width of the levees deposited at the lateral extents of the avalanche is a useful way to distinguish between the different behaviours. A plot of the levee width with downslope position is shown in Fig. 4(b) for a 10 mL volume release at various slope angles. An avalanche is considered to be decaying when the reduction in the width between the levees, from crest-to-crest, is greater than 5% without any shedding of material. This occurs for $\zeta = 33.0°$ and $\zeta = 33.5°$ as shown in Fig. 4(b). There are steady-states at $\zeta = 34.0°$ and $\zeta = 34.5°$, characterised by a constant width between the levees being maintained as the avalanche propagates downslope. At a slope angle of 35.0°, the width of the avalanche formed from a 10 mL volume release decreases. However, in this case, the slope angle is sufficiently steep that the avalanche actually breaks and sheds some material, resulting in a sudden decrease in width before a constant distance between the levees is attained. The initial volume is therefore too large at that slope angle (see Fig. 4a) for the avalanche to reach a steady-state, hence it must shed excess material and re-adjust its width in order to do so. However, this re-adjustment toward a steady-state can be a continuous process that takes a long distance to occur, as observed at an even steeper slope angle of $\zeta = 35.5°$. Once again the initial mass released is too big to lead immediately to a steady-state and the avalanche sheds mass in its tail. However, over a distance of 1 m a steady travelling wave is still not reached at this steeper slope angle and so the width between the levees decreases continuously. This readjustment of large waves, by shedding mass or splitting into several smaller waves, could have important consequences on the design of dams to deflect or stop the flow.

Fig. 4(c) to (f) shows a typical experiment for each of four distinct avalanche behaviours observed as a function of the volume released and the slope angle. Regardless of the regime in which the avalanche propagates, the initial yellow sand released is always deposited during the propagation, leading to an avalanche mostly consisting of particles from the erodible bed. This is particularly true for the decaying and steady propagating avalanche (Fig. 4c and d). If the volume released is too big or the slope angle too steep, the avalanche sheds and looses mass during its propagation as it re-adjust to a travelling steady wave (Fig. 4e). In extreme cases, the amount of shed material can be so large that the excess grains have enough momentum to form secondary waves in the tail of the original avalanche. These secondary waves can in some cases propagate over a long distance before they come to rest as small deposits between the levees of the main flow (Fig. 4f). For both shedding processes, i.e. both those that generate secondary waves and those that do not, the shape of the first avalanche is longer and thinner than that of a steady propagating one, allowing more mass to be deposited in its wake. Furthermore, yellow particles from the initial release are still present near the end of the plane in the shedding avalanches, implying that the erosion-deposition process is less pronounced for high velocity avalanches where grains from the initial release remain in the avalanche for a longer distance.

4. A depth-averaged erosion-deposition model

Despite the fundamental differences between debris flows, pyroclastic flows and avalanches, one similarity is that the depths of these flows are small compared to their lengths. This observation implies that all of these types of flows may be considered shallow and can therefore be modelled in a depth-averaged framework. A formal derivation of the shallow water-type equations used to model geophysical mass flows was first developed by Savage and Hutter (1989). Using a Mohr-Coulomb internal rheology and constant Coulomb basal friction law, they successfully applied their equations to the motion of a finite mass of granular material on a variable slope (Savage and Hutter, 1991). Since then, the Savage-Hutter model has been extended to two-dimensional flows over complex topography with applications in snow avalanches (Cui et al., 2007), debris flows (Iverson, 1997), pyroclastic flows (Pitman et al., 2003) and landslides (Mangeney et al., 2010).

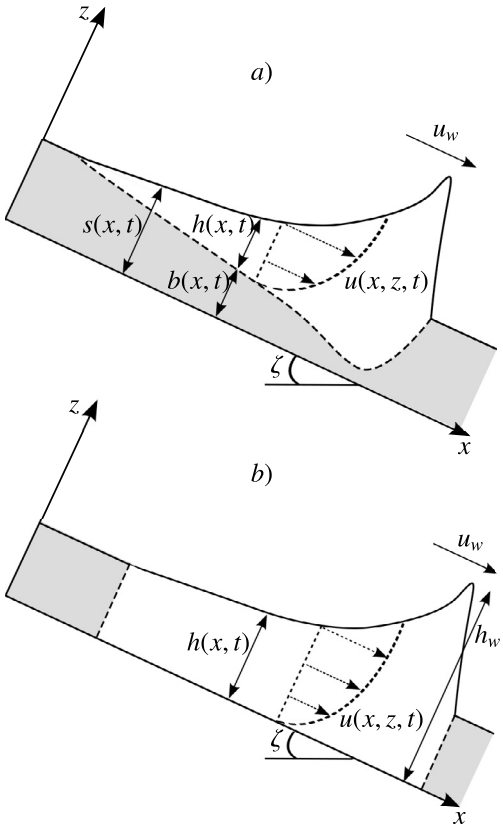

Fig. 5. Schematic diagram showing two possible representations of the erosion-deposition process in shallow granular avalanches.

Modelling the balance between erosion and deposition in granular flows remains a challenging issue. Adopting a depth-averaged approach, there are (at least) two ways of modelling the erosion-deposition process. One may take into account only the mobile grains by defining the avalanche depth $h(x,t)$ as the thickness normal to the plane between the free-surface $s(x,t)$ and the interface $b(x,t)$ that separates mobile and static regions (see Fig. 5a). Whilst this representation may accurately describe the dynamics of a granular flow on an erodible bed, it is difficult to simulate because an unknown expression for the erosion/deposition rate at the base of the avalanche is needed to close the system (Douady et al., 1999; Gray, 2001; Gray and Ancey, 2001; Iverson, 2012). As such, an alternative way to model the erosion-deposition process is to assume a complete mobilisation of the flow throughout the entire depth (see Fig. 5b). This was first developed by Pouliquen and Forterre (2002), who defined a basal friction $\mu(h, Fr)$ for the whole range of possible flow thicknesses and Froude numbers. Their model implies that the flow is either completely mobile or completely static throughout its depth at any particular point. Although this may seem to be a crude approximation, they found good agreement with their experiments for the release of mass on erodible slopes. This approach has also recently been used by Edwards and Gray (2015) and modified by Edwards et al. (2017, 2019) to successfully simulate both two- and three-dimensional erosion-deposition waves observed in experiments. It is the latter approach that is used here to model our avalanches.

4.1. Depth-averaged equations with viscous dissipation

For an avalanche of thickness h and depth-averaged velocity $\bar{\boldsymbol{u}} = (\bar{u}, \bar{v})$, the depth-averaged mass and momentum balance equations are derived by a two-dimensional extension of the depth-averaged $\mu(I)$-rheology (Gray and Edwards, 2014; Baker et al., 2016a; Edwards et al., 2017), and are given here as

$$\frac{\partial h}{\partial t} + \frac{\partial}{\partial x}(h\bar{u}) + \frac{\partial}{\partial y}(h\bar{v}) = 0, \tag{3}$$

$$\frac{\partial}{\partial t}(h\bar{u}) + \frac{\partial}{\partial x}(h\bar{u}^2) + \frac{\partial}{\partial y}(h\bar{u}\bar{v}) + \frac{\partial}{\partial x}\left(\frac{1}{2}h^2 g\cos\zeta\right) = hgS^x + V^x(x,y), \tag{4}$$

$$\frac{\partial}{\partial t}(h\bar{v}) + \frac{\partial}{\partial x}(h\bar{u}\bar{v}) + \frac{\partial}{\partial y}(h\bar{v}^2) + \frac{\partial}{\partial y}\left(\frac{1}{2}h^2 g\cos\zeta\right) = hgS^y + V^y(x,y), \tag{5}$$

where the shape factor $\overline{u^2}/\bar{u}^2$ resulting from the depth-integration is assumed to be unity for simplicity (Savage and Hutter, 1989; Gray et al., 1999; Pouliquen, 1999a; Pouliquen and Forterre, 2002; Gray et al., 2003). The source terms

$$S^x = \sin\zeta - \mu\frac{\bar{u}}{|\bar{\mathbf{u}}|}\cos\zeta, \tag{6}$$

$$S^y = -\mu\frac{\bar{v}}{|\bar{\mathbf{u}}|}\cos\zeta, \tag{7}$$

consist of the component of gravity in the downslope x-direction and the effective basal friction $\mu = \mu(h, \mathrm{Fr})$ between the avalanche and the rough plane, which opposes the direction of motion. Edwards et al. (2017, 2019) derived the following friction coefficient for angular particles (e.g. sand, carborundum), which is adopted here,

$$\mu = \begin{cases} \mu_d & Fr > \beta_*, \\ \mu_i & 0 < Fr < \beta_*, \\ \mu_s & Fr = 0, \end{cases}$$

where

$$\mu_d = \mu_1 + \frac{\mu_2 - \mu_1}{1 + h\beta/(\mathscr{L}(\mathrm{Fr} + \Gamma))}, \tag{8}$$

$$\mu_i = \left(\frac{\mathrm{Fr}}{\beta_*}\right)^{\kappa}\left(\mu_1 + \frac{\mu_2 - \mu_1}{1 + h\beta/(\mathscr{L}(\beta_* + \Gamma))} - \mu_3 - \frac{\mu_2 - \mu_1}{1 + h/\mathscr{L}}\right) + \mu_3 + \frac{\mu_2 - \mu_1}{1 + h/\mathscr{L}}, \tag{9}$$

$$\mu_s = \min\left(\mu_3 + \frac{\mu_2 - \mu_1}{1 + h/\mathscr{L}}, |\tan\zeta\boldsymbol{i} - \nabla h|\right). \tag{10}$$

The constants $\mu_1 = \tan\zeta_1$, $\mu_2 = \tan\zeta_2$ and $\mu_3 = \tan\zeta_3$ are the tangents of the critical angles, ζ_1, ζ_2 and ζ_3. The parameter $\beta_* > \max(\beta - \Gamma, 0)$ was introduced by Edwards et al. (2017) as the Froude number of the slowest observable steady uniform flow, in order to correctly match the thickness h_{stop} of a deposit layer.

The viscous rheology terms in the x- and y-momentum equations are

$$V^x(x,y) = \frac{\partial}{\partial x}\left(\nu h^{3/2}\frac{\partial\bar{u}}{\partial x}\right) + \frac{\partial}{\partial y}\left(\frac{1}{2}\nu h^{3/2}\left(\frac{\partial\bar{v}}{\partial x} + \frac{\partial\bar{u}}{\partial y}\right)\right), \tag{11}$$

$$V^y(x,y) = \frac{\partial}{\partial x}\left(\frac{1}{2}\nu h^{3/2}\left(\frac{\partial\bar{u}}{\partial y} + \frac{\partial\bar{v}}{\partial x}\right)\right) + \frac{\partial}{\partial y}\left(\nu h^{3/2}\frac{\partial\bar{v}}{\partial y}\right), \tag{12}$$

where the coefficient

$$\nu = \frac{2}{9}\frac{\mathscr{L}\sqrt{g}}{\beta}\frac{\sin\zeta}{\sqrt{\cos\zeta}}\left(\frac{\tan\zeta_2 - \tan\zeta}{\tan\zeta - \tan\zeta_1}\right), \tag{13}$$

in the effective viscosity $\nu h^{1/2}/2$ is determined explicitly in the depth-integration process (Gray and Edwards, 2014).

The mass and momentum balance equations are supplemented with an additional equation for the interface between yellow and red sand. The two-dimensional equivalent of the large-particle transport equation developed by Gray and Kokelaar (2010),

$$\frac{\partial\eta}{\partial t} + \frac{\partial}{\partial x}\left(\eta\bar{u} - (1-\alpha)\bar{u}\eta\left(1 - \frac{\eta}{h}\right)\right) + \frac{\partial}{\partial y}\left(\eta\bar{v} - (1-\alpha)\bar{v}\eta\left(1 - \frac{\eta}{h}\right)\right) = 0, \tag{14}$$

was originally derived for the evolution of the inversely graded shock interface $\eta = h\bar{\phi}$ between a sharply segregated layer of large particles above a layer of small particles in a bidisperse mixture, where $\bar{\phi}$ is the depth-averaged small-particle concentration. This theory is applied to our monodisperse flow where $z = \eta$ instead represents a sharp interface between red and yellow sand and $\bar{\phi} = \eta/h$ is the depth-averaged red particle concentration. The parameter $0 \le \alpha \le 1$ allows the downslope velocity profile to vary from simple shear for $\alpha = 0$ to plug flow for $\alpha = 1$ and linear shear with basal slip for values in-between. A value of $a = 1/7$ is taken here, since it was shown by Baker et al. (2016b) to closely approximate a Bagnold velocity profile, at least for depth-averaged quantities.

4.2. Numerical results

The mass and momentum balance equations (3)–(5) coupled with the sand colour interface equation (14) are written in conservative vector form and solved for a system that replicates the experimental setup. The numerical method used to solve the model is a semi-discrete high-resolution non-oscillatory central scheme of Kurganov and Tadmor (2000) together with a second order Runge-Kutta method for their time evolution. More details about the numerical model can be found in Edwards et al. (2017). The initial conditions here are of a cylindrical pile of sand, with radius $R = 1.5$ cm and a height that provides the desired volume, centred at $(x, y) = (0, 0)$ on top of a static layer of thickness $h_0 = h_{stop}(\zeta)$ at a slope angle ζ. The pile is prescribed a yellow colour and the static layer red by setting the initial interface position as $\eta(x, y, 0) = h_0$. Zero initial momentum is set with $h\bar{u}(x, y, 0) = h\bar{v}(x, y, 0) = 0$. Free outflow is imposed at the downstream boundary via a linear extrapolation of the values of h, $h\bar{u}$ and η from the final two columns of interior cells and a stationary inflow of red sand is imposed at the upstream boundary by $h(0, y, t) = h_0$, $h\bar{u}(0, y, t) = h\bar{v}(0, y, t) = 0$ and $\eta(0, y, t) = h_0$.

The results of a typical numerical simulation at a slope angle of $\zeta = 34.0°$ and a 10 mL volume of yellow sand released on top of a stationary layer of red sand with thickness $h_0 = h_{stop}(34°) = 1.7$ mm are shown in Fig. 6(b)–(f) at various times. The colouring is based on the value of the depth-averaged concentration of red particles $0.6 \le \bar{\phi} \le 1.0$. As in the experiments, a first simulation has been performed on an empty bed (see Fig. 6a) leading to a similar deposit over ~ 15cm. For the simulation involving an erodible layer, the avalanche initially spreads before propagating steadily whilst depositing levees at the lateral extents of the flow head, as observed in the experiments. Moreover, towards the end of the domain almost all the initial yellow particles have been deposited and the avalanche is composed almost entirely of red particles. The mean width $W = 10$ cm between the levees from crest-to-crest and the speed of propagation $u_w = 0.21$ m.s^{-1} of the avalanche in the simulation are both in good agreement with the experimentally measured values of $W \approx 9$ cm and $u_w = 0.19$ m.s^{-1}, respectively.

To further investigate the reliability of the model, several simulations have been performed with different volumes of material

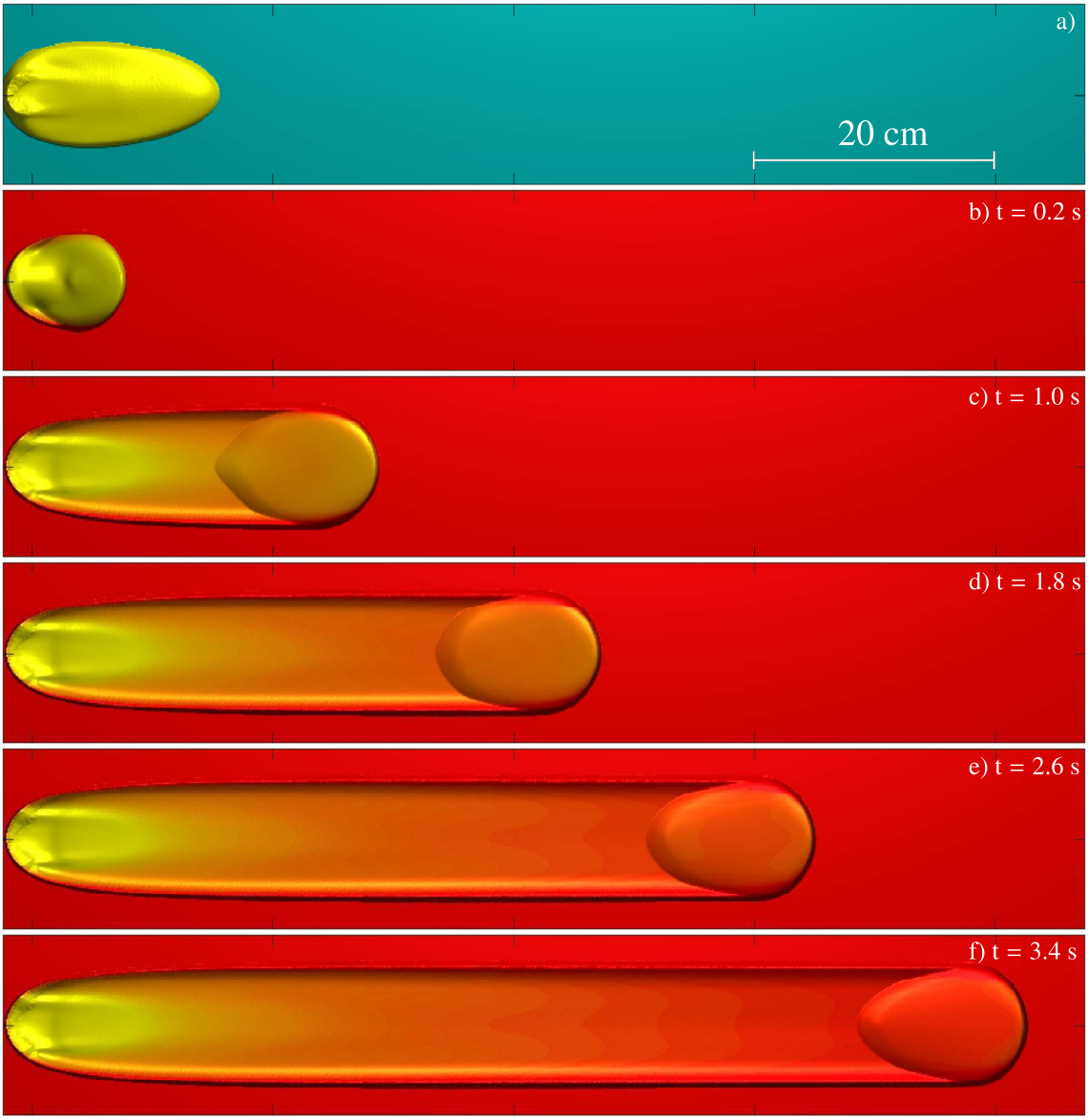

Fig. 6. Numerical simulation of the propagation of a single avalanche on a 34.0° slope a) without an erodible layer (final deposit), b)–f) with an erodible layer. The depth-averaged concentration of red particles is shown with a contour scale, which is designed to match the experimental images, and ranges from yellow at $\bar{\phi} = 0.6$ to red at $\bar{\phi} = 1$. In addition, an impression of the thickness variation is shown by using oblique lighting from the top left of each panel to light the three-dimensional free-surface and show the levees and the front. As in the experiment, all of the initially released yellow sand is deposited during the propagation to produce a steady propagating avalanche that is composed entirely of red particles from the erodible layer.

released at various slope angles in order to reproduce the different avalanche behaviours observed in the experiments. All four of the experimentally observed behaviours; namely decay, steady, shedding and extreme shedding with secondary waves, have been reproduced in Fig. 7 by numerically replicating the initial conditions of the corresponding experiments (see Fig. 4). The numerical results are in very good agreement with the experiments for each behaviour. In particular, for the shedding cases (Fig. 7c and d) the shape of the avalanche differs from the steady case, as observed in the experiments. Moreover, the rate of colour change varies in the simulations with the yellow particles being transported further downslope by the shedding avalanches, which was also observed in the experiments.

5. Application to debris flows on the Moon

Recently Kokelaar et al. (2017) identified three types of debris-flow deposits in several lunar craters where they formed without any influence of atmosphere or liquid. Two of these deposit types, (i) multiple channels with coarse-grained levees and lobate terminations and (ii) single-surge polylobate, are common on Earth, formed by geophysical phenomena such as pyroclastic flows and avalanches. However, the third type of deposit observed on the Moon has no known equivalent on Earth. It consists of a narrow, low-profile and long ribbon, with reworked substrate, minor levees and no coarse terminations. Such deposits typically occur in multiple sets and have been interpreted to result from the propagation of granular erosion-deposition waves down repose slopes of fine-grained erodible regolith.

Fig. 8 shows the novel debris-flow deposits in the Virtanen F crater. From source to termination the runout distance is about 4.5 km. Due to subtle topographical effects inducing either convergence or divergence and many bifurcations, it is not clear whether a single flow splits into two or whether a later flow has escaped from the path of its predecessor. In either scenario, however, these deposits commonly exhibit extreme length-to-width ratios of kilo-

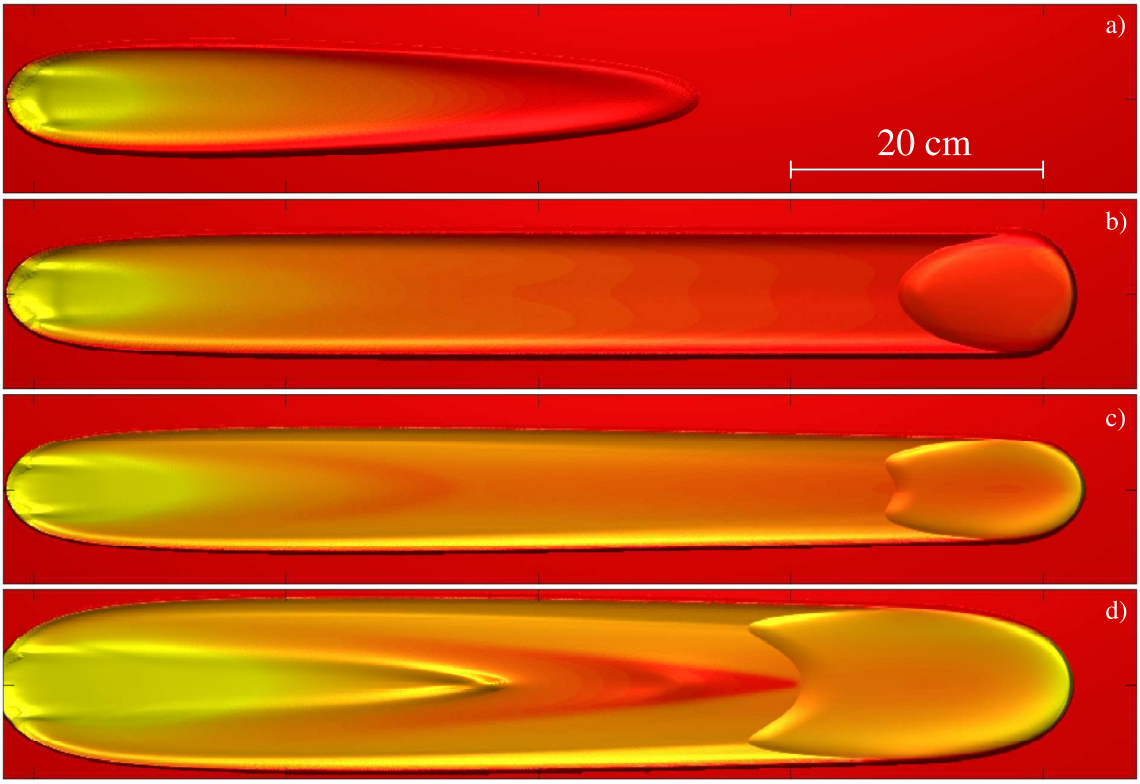

Fig. 7. Numerical simulations for the propagation of a single avalanche exhibiting different behaviour: a) 10 mL at 33° - decaying, b) 10 mL at 34° - steady, c) 10 mL at 35.8° - shedding and d) 20 mL at 35.5°: extreme shedding with secondary waves. The yellow sand is transported further downslope by the shedding avalanches. Note that any asymmetry in colour in the y-direction is simply an artificial lighting effect. Movie of the simulations for each behaviours is available in the online supplementary material (movie 5).

meters in length versus only a few meters in width, persistent ribbon-like parallelism of margins that generally lack obvious levees, absence of mounded coarse-grained terminations and considerable sensitivity to slope changes. The dark albedo of the flow tracks is attributed to erosion, mixing and re-deposition of slope substrate during the passage of waves. Kokelaar et al. (2017) infer that the pale substrate is mainly fine-grained regolith with underlying less-degraded debris. Thus the dark tracks may be mixed and re-deposited material that is somewhat coarser and less smooth, which appears darker than adjacent surface material.

The characteristics of these deposits in the Virtanen F crater are very similar to those produced by our experimental erosion-deposition waves. Moreover, as in the experimental procedure, the formation of these deposits on the Moon seems to relate to small-volume triggering flows released onto and travelling far down a mature repose slope.

In their account of the lunar deposits, Kokelaar et al. (2017) proposed that the erosion-deposition waves may be favored on the Moon surface by the abundance there of relatively fine material at repose angle, with the granular dilatation facilitated by the lack of interstitial fluid. Thus, all of the physical mechanisms identified in our laboratory experiments, which explain erosion-deposition waves in dry granular flows, remain valid on the surface of the Moon. The conditions on the Moon serve to make the mechanisms easier to operate and the deposits more likely to be preserved than in nature on Earth.

6. Conclusion

In this paper multiple steady travelling waves states have been observed in the avalanches that form when a finite mass of sand particles is released on a rough plane covered with an erodible layer of the same grains. Moreover, different types of behaviour are also possible depending on the volume of material that is released and the inclination of the bed. For sufficiently shallow slopes and thick erodible layers, the avalanche continuously decays in size, thus only travelling for a finite distance downslope before coming to rest. By increasing either the volume released, the slope angle or both, a steadily propagating avalanche can be generated in which there is a perfect balance between erosion and deposition of grains. For even steeper slopes and/or bigger volumes of mass released, the avalanches that form are too large to remain steady and shed excess mass until they become steady. In extreme cases, the amount of shed material is sufficient for itself to gain momentum and develop into secondary waves in the tail of the leading avalanche. In all the cases, the presence of an erodible layer drastically increases the runout distances of the flow, as observed previously in several experiments (Pouliquen and Forterre, 2002; Mangeney et al., 2007; Farin et al., 2014).

By releasing material of one colour onto an erodible bed of another, this paper also presents the finding that the particles from the initial release are all deposited during the propagation of the avalanche. Although an avalanche can propagate steadily with a constant shape and speed over the 120 cm length of our plane, the initial release of sand is mostly deposited over a distance of about 60 cm, resulting in an avalanche composed almost exclusively of particles from the erodible bed. These are the first experiments where an exchange between particles from a bulk flow and particles from an erodible bed is clearly visible. For steeper slope angles on which shedding avalanches are formed, the initially released grains are transported further downslope than in the steady or decaying cases. All of these observations can have important consequences on field measurement and the composition of the deposit observed after natural hazards.

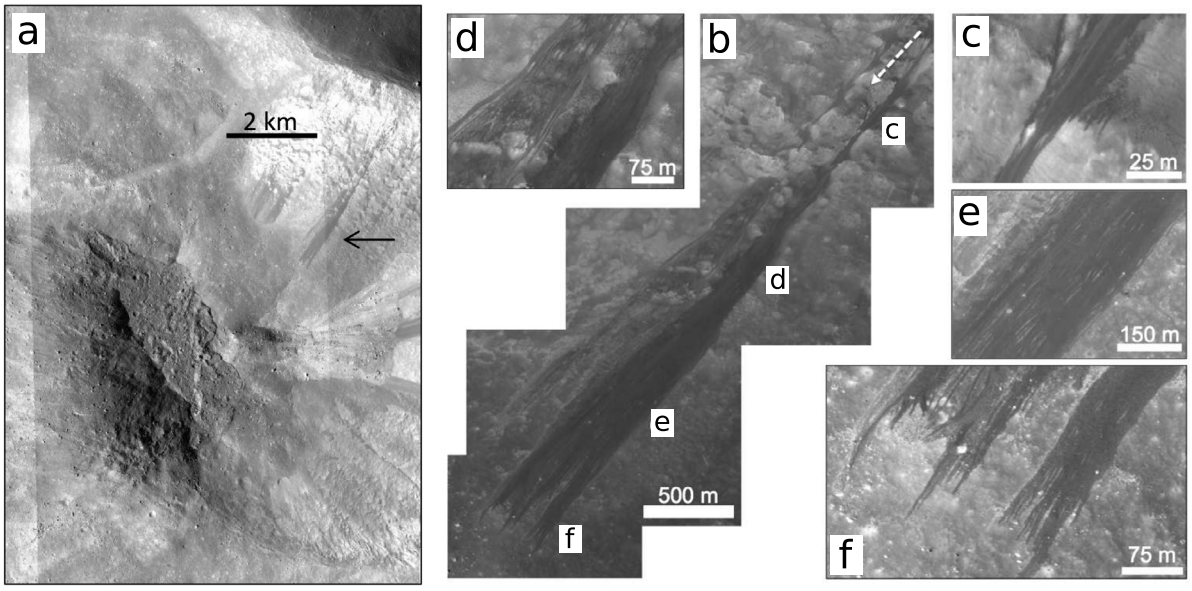

Fig. 8. a) Virtanen F crater showing the location (arrow) of debris-flow deposits detailed in figures b-f. The deposits are distinctive for their darker colour than the underlying substrate and manifestly multiple nature in lower reaches, where there are several tens of remarkably continuous narrow fingers. These deposits and similar ones nearby to the left are restricted to repose slopes. The extensive degraded lobate deposits on the mid left are from flows of impact-melt that reached the crater floor. Image from https://quickmap.lroc.asu.edu courtesy of NASA/GSFC/ASU (from Kokelaar et al. (2017)). b) Entire runout from just beneath the source(s), showing locations of detail panels c-f. c) Deposit trails are locally confluent according to topographic constriction. d) Flow paths diverge on slightly lesser slopes, locally originating from streaked pale slopes presumed to be dominantly sites of material overpassing. e) Tens of narrow, ribbon-like fingers become distinct where the slope is less irregular. The ribbon-like flow units are mostly sub-parallel. f) Flow-unit terminations are abruptly rounded or tapered and appear in bundles, there are no (distinct) levees or terminal mounded accumulations. LROC NAC image M169398317LE courtesy of NASA/GSFC/ASU.

Numerical simulations using a shallow granular avalanche model resulting from a two-dimensional generalisation (Baker et al., 2016a) of the depth-averaged $\mu(I)$-rheology (Gray and Edwards, 2014), with Edwards et al.'s (2019) friction coefficient, are in good qualitative agreement with the experiments. All of the different types of avalanche behaviours are generated by reproducing the experimental configurations. Moreover, the rate of colour change, tracked by the large-particle transport equation of Gray and Kokelaar (2010) for the interface between two distinct colours in a monodisperse flow, is also well captured by the model. This means that the kinematic motion of grains in such avalanches can be approximated by an advection process with a preferential shearing of particles at the surface to the flow front.

Debris-flows deposits observed in lunar craters by Kokelaar et al. (2017) show strikingly similar characteristics to the laboratory experiments presented here. The extreme runout distance reached by apparently small-volume flows, without elevated levees and absence of mounded coarse-grained terminations, has been interpreted as registering the passage of erosion-deposition waves. It is easy to imagine that all four of the different propagation regimes observed in the experiments can occur in a single natural flow due to topographic effects. The avalanche starts to shed its mass on steep slopes, propagates steadily on slopes close to the angle of repose and finally decays and stops on shallow slopes. These same physical mechanisms have been interpreted by Kokelaar et al. (2017) to be responsible for the deposits on the Virtanen F crater.

Acknowledgements

This research was supported by NERC grants NE/E003206/1 and NE/K003011/1 as well as EPSRC grants EP/I019189/1, EP/K00428X/1 and EP/M022447/1. J. M. N. T. Gray is a Royal Society Wolfson Researcher Merit Award holder (WM150058) and an EPSRC Established Career Fellow (EP/M022447). All research data supporting this publication are directly available within this publication.

Appendix A. Supplementary material

Supplementary material related to this article can be found online at https://doi.org/10.1016/j.epsl.2019.07.003.

References

Baker, J.L., Barker, T., Gray, J.M.N.T., 2016a. A two-dimensional depth-averaged $\mu(I)$-rheology for dense granular avalanches. J. Fluid Mech. 787, 367–395.
Baker, J.L., Johnson, C.G., Gray, J.M.N.T., 2016b. Segregation-induced finger formation in granular free-surface flows. J. Fluid Mech. 809, 168–212.
Berger, C., McArdell, B.W., Schlunegger, F., 2011. Direct measurement of channel erosion by debris flows, illgraben, Switzerland. J. Geophys. Res., Earth Surf. 116 (F1).
Bouchut, F., Westdickenberg, M., 2004. Gravity driven shallow water models for arbitrary topography. Commun. Math. Sci. 2 (3), 359–389.
Conway, S.J., Decaulne, A., Balme, M.R., Murray, J.B., Towner, M.C., 2010. A new approach to estimating hazard posed by debris flows in the westfjords of Iceland. Geomorphology 114 (4), 556–572.
Cui, X., Gray, J.M.N.T., 2013. Gravity-driven granular free-surface flow around a circular cylinder. J. Fluid Mech. 720, 314–337.
Cui, X., Gray, J.M.N.T., Johannesson, T., 2007. Deflecting dams and the formation of oblique shocks in snow avalanches at Flateyri, Iceland. J. Geophys. Res. 112, F04012.
Delannay, R., Valance, A., Mangeney, A., Roche, O., Richard, P., 2017. Granular and particle-laden flows: from laboratory experiments to field observations. J. Phys. D, Appl. Phys. 50 (5), 053001.
Douady, S., Andreotti, B., Daerr, A., 1999. On granular surface flow equations. Eur. Phys. J. B 11, 131–142.
Edwards, A.N., Gray, J.M.N.T., 2015. Erosion-deposition waves in shallow granular free-surface flows. J. Fluid Mech. 762, 35–67.
Edwards, A.N., Russell, A.S., Johnson, C.G., Gray, J.M.N.T., 2019. Frictional hysteresis and particle deposition in granular free-surface flows. J. Fluid Mech. https://doi.org/10.1017/jfm.2019.517. In press.
Edwards, A.N., Viroulet, S., Kokelaar, B.P., Gray, J.M.N.T., 2017. Formation of levees, troughs and elevated channels by avalanches on erodible slopes. J. Fluid Mech. 823, 278–315.
Farin, M., Mangeney, A., Roche, O., 2014. Fundamental changes of granular flow dynamics, deposition, and erosion processes at high slope angles: insights from laboratory experiments. J. Geophys. Res., Earth Surf. 119 (3), 504–532.
Forterre, Y., 2006. Kapiza waves as a test for three-dimensional granular flow rheology. J. Fluid Mech. 563, 123–232.
Forterre, Y., Pouliquen, O., 2003. Long-surface-wave instability in dense granular flows. J. Fluid Mech. 486, 21–50.

Gray, J.M.N.T., 2001. Granular flow in partially filled slowly rotating drums. J. Fluid Mech. 441, 1–29.

Gray, J.M.N.T., Ancey, C., 2001. Segregation, recirculation and deposition of coarse particles near two-dimensional avalanche fronts. J. Fluid Mech. 629, 387–423.

Gray, J.M.N.T., Edwards, A.N., 2014. A depth-averaged $\mu(I)$-rheology for shallow granular free-surface flows. J. Fluid Mech. 755, 503–534.

Gray, J.M.N.T., Kokelaar, B.P., 2010. Large particle segregation, transport and accumulation in granular free-surface flows. J. Fluid Mech. 652, 105–137.

Gray, J.M.N.T., Tai, Y.C., Noelle, S., 2003. Shock waves, dead-zones and particle-free regions in rapid granular free-surface flows. J. Fluid Mech. 491, 161–181.

Gray, J.M.N.T., Thornton, A.R., 2005. A Theory for Particle Size Segregation in Shallow Granular Free-Surface Flows, vol. 461. The Royal Society, pp. 1447–1473.

Gray, J.M.N.T., Wieland, M., Hutter, K., 1999. Gravity-driven free surface flow of granular avalanches over complex basal topography. Proc. R. Soc. Lond. A 455, 1841–1874.

Iverson, R.M., 1997. The physics of debris-flows. Rev. Geophys. 35, 245–296.

Iverson, R.M., 2012. Elementary theory of bed-sediment entrainment by debris flows and avalanches. J. Geophys. Res. 117, F03006.

Iverson, R.M., Reid, M.E., Logan, M., LaHusen, R.G., Godt, J.W., Griswold, J.P., 2011. Positive feedback and momentum growth during debris-flow entrainment of wet bed sediment. Nat. Geosci. 4 (2), 116–121.

Johnson, C.G., Kokelaar, B.P., Iverson, R.M., Logan, M., LaHusen, R.G., Gray, J.M.N.T., 2012. Grain-size segregation and levee formation in geophysical mass flows. J. Geophys. Res. 117, F01032.

Jop, P., Forterre, Y., Pouliquen, O., 2006. A constitutive law for dense granular flows. Nature 441 (7094), 727–730.

Kelfoun, K., Druitt, T.H., 2005. Numerical modeling of the emplacement of socompa rock avalanche, Chile. J. Geophys. Res., Solid Earth 110. B12.

Kokelaar, B.P., Bahia, R.S., Joy, K.H., Viroulet, S., Gray, J.M.N.T., 2017. Granular avalanches on the moon: Mass-wasting conditions, processes and features. J. Geophys. Res., Planets 122, 1893–1925.

Kokelaar, B.P., Graham, R.L., Gray, J.M.N.T., Vallance, J.W., 2014. Fine-grained linings of leveed channels facilitate runout of granular flows. Earth Planet. Sci. Lett. 385, 172–180.

Kurganov, A., Tadmor, E., 2000. New high-resolution central schemes for nonlinear conservation laws and convection-diffusion equations. J. Comput. Phys. 160, 241–282.

Mangeney, A., Bouchut, F., Thomas, N., Vilotte, J.P., Bristeau, M.O., 2007. Numerical modeling of self-channeling granular flows and of their levee-channel deposits. J. Geophys. Res. 112, F02017.

Mangeney, A., Roche, O., Hungr, O., Magnold, N., Faccanoni, G., Lucas, A., 2010. Erosion and mobility in granular collapse over sloping beds. J. Geophys. Res. 115, F03040.

Moretti, L., Allstadt, K., Mangeney, A., Capdeville, Y., Stutzmann, E., Bouchut, F., 2015. Numerical modeling of the mount meager landslide constrained by its force history derived from seismic data. J. Geophys. Res., Solid Earth 120 (4), 2579–2599.

Pitman, E.B., Nichita, C.C., Patra, A., Bauer, A., Sheridan, M., Bursik, M., 2003. Computing granular avalanches and landslides. Phys. Fluids 15, 3638–3646.

Pouliquen, O., 1999a. On the shape of granular fronts down rough inclined planes. Phys. Fluids 11 (7), 1956–1958.

Pouliquen, O., 1999b. Scaling laws in granular flows down rought inclined planes. Phys. Fluids 11 (3), 542–548.

Pouliquen, O., Delour, J., Savage, S.B., 1997. Fingering in granular flows. Nature 386 (6627), 816.

Pouliquen, O., Forterre, Y., 2002. Friction law for dense granular flows: application to the motion of a mass down a rough inclined plane. J. Fluid Mech. 453, 133–151.

Savage, S.B., Hutter, K., 1989. The motion of a finite mass of granular material down a rough incline. J. Fluid Mech. 199, 177–215.

Savage, S.B., Hutter, K., 1991. The dynamics of avalanches of granular materials from initiation to run-out. I. Analysis. Acta Mech. 86, 201–223.

Viroulet, S., Baker, J.L., Edwards, A.N., Johnson, C.G., Gjaltema, C., Clavel, P., Gray, J.M.N.T., 2017. Multiple solutions for granular flow over a smooth two-dimensional bump. J. Fluid Mech. 815, 77–116.

Viroulet, S., Baker, J.L., Rocha, F.M., Johnson, C.G., Kokelaar, B.P., Gray, J.M.N.T., 2018. The kinematics of bidisperse granular roll waves. J. Fluid Mech. 848, 836–875.

Woodhouse, M.J., Thornton, A.R., Johnson, C.G., Kokelaar, B., Gray, J.M.N.T., 2012. Segregation-induced fingering instabilities in granular free-surface flows. J. Fluid Mech. 709, 543–580.